



Sustainable oxidation catalysis supported by light: Fe-poly (heptazine imide) as a heterogeneous single-atom photocatalyst

Marcos A.R. da Silva^{a,1}, Ingrid F. Silva^{b,c,1}, Qi Xue^d, Benedict T.W. Lo^d, Nadezda V. Tarakina^c, Barbara N. Nunes^{e,j}, Peter Adler^f, Sudhir K. Sahoo^g, Detlef W. Bahnemann^e, Nieves López-Salas^c, Aleksandr Savateev^c, Caue Ribeiro^h, Thomas D. Kühne^{g,i}, Markus Antonietti^c, Ivo F. Teixeira^{a,c,*}

^a Department of Chemistry, Federal University of São Carlo, 13565-905, São Carlos, SP, Brazil

^b Department of Chemistry, ICEX, Federal University of Minas Gerais, 31270-901, Belo Horizonte, MG, Brazil

^c Department of Colloid Chemistry, Max Planck Institute of Colloids and Interfaces, Am Mühlenberg 1, D-14476 Potsdam, Germany

^d State Key Laboratory of Chemical Biology and Drug Discovery, Department of Applied Biology and Chemical Technology, The Hong Kong Polytechnic University, Hungghom, Hong Kong, China

^e Institut für Technische Chemie, Leibniz Universität Hannover, Callinstrasse 3, D-30167, Hannover, Germany

^f Max Planck Institute for Chemical Physics of Solids, 01187 Dresden, Germany

^g Dynamics of Condensed Matter and Center for Sustainable System Design, Chair of Theoretical Chemistry, University of Paderborn, Warburger Str. 100, D-33098 Paderborn, Germany

^h National Nanotechnology Laboratory for Agriculture, Brazilian Agriculture Research Corporation (Embrapa), XV de Novembro Street – 1452, São Carlos, Brazil

ⁱ Paderborn Center for Parallel Computing and Institute for Lightweight Design, University of Paderborn, Warburger Str. 100, D-33098 Paderborn, Germany

^j Laboratory of Photochemistry and Materials Science, Federal University of Uberlândia, 38400-902 Uberlândia, MG, Brazil

ARTICLE INFO

Keywords:

Single-atom catalysis
Photooxidation
Benzene Oxidation
Iron
Poly (heptazine imide)

ABSTRACT

Fe-N-C materials, when prepared as single-atom catalysts (SAC), display excellent activities in oxidation reactions. The systematic investigation of the iron coordination mode revealed that Fe-N₄C catalysts are the most active for C-H bond oxidation. However, many of these catalysts are synthesized through pyrolysis, which is characterized by a lack of control and structures with heterogeneous composition, rarely presenting only atomically dispersed Fe-N – C as active sites. Herein, an alternative, reliable and easily reproducible method to obtain highly active Fe SACs (atomically dispersed) with Fe-N₄ sites is presented, which is based on ion exchange of sodium from high crystalline sodium poly(heptazine imide) (Na-PHI) by other ions. The obtained catalyst can photocatalytically oxidize C-H bonds selectively toward ketones using only dioxygen. Detailed mechanism investigations indicate that the active species in the C-H bond oxidation are highly valent Fe(IV)/Fe(V)-oxo species, which are further activated by the holes generated at the PHI support under light irradiation.

1. Introduction

Single-atom heterogeneous catalysis (SAC) is often called “the missing link between homogeneous and heterogeneous catalysis”. A large body of publications in the last decade have shown the possibility of uniting the robustness of heterogeneous systems with the well-defined metal environment of homogeneous catalysts in SAC, and it definitely depends on new tools of nanoscale synthesis and analytics. The field of single-atoms catalysis has for instance been limited by the resolution of the analytical methods, and only with the recent gains, it has become

possible to investigate the single-atoms sites in a more systematic way [1,2]. However, already the first decade of SAC research showed that it can play a pivotal role in improved chemical synthesis, as it provides an atomic distribution and unique reactivity of metals in immobile, stable, and robust hosts [1,3–7]. The presence of isolated atoms enhances the catalytic turnover frequency, which is important to reduce the amount of transition metals required by a reaction, while the supported character improves lifetime and recyclability [1,4–6].

Several materials were applied as supports for single-atoms, such as zeolites [8–12], graphene [10,13], N-doped carbons [14–17],

* Corresponding author at: Department of Chemistry, Federal University of São Carlo, 13565-905, São Carlos, SP, Brazil.

E-mail address: ivo@ufscar.br (I.F. Teixeira).

¹ MARS and IFS contributed equally to this work.

metal-organic frameworks [18–21], and carbon nitrides [22–31]. In particular, metal- N_x coordination sites are among the most investigated systems for SAC, as they can anchor and stabilize metal atoms firmly and tune the metal properties according to coordination geometry and nitrogen electron density [14,15,22–24,32,33]. In general, these catalytic systems use N-doped carbons as hosts, which face often problems in terms of structural organization. [14,15] As stated by Zhang et al. “M–N–C materials are heterogeneous in both composition and particle size as a result of an uncontrollable pyrolysis process. In fact, in many cases multispecies of M, such as metallic M nanoparticles, MO_x nanoparticles, and monodispersed as well as aggregated M– N_x species are simultaneously present in one system [34–37], which poses significant challenges for the identification and quantification of the active site” [38].

Just recently, poly(heptazine imides) (PHI) have emerged as a highly ordered and crystalline host option for SAC (Fig. S1a). Pérez-Ramírez et al. have reported a successful use of poly(heptazine imide)s and poly(triazine imide)s (PTIs) as scaffolds to stabilize Pd single-atoms [24]. PHI-based materials are of particular interest, as they are crystalline with a well-defined structure where negative poly(heptazine imide) 2D-layers are charge-compensated by Na^+ or K^+ cations [39,40]. The possibility to exchange alkali ions in the matrix by some transition metals (i.e., Mg, Co, Ni, Ru, Pt and Ag) was investigated by Savateev et al. [41] and Colombari et al. [42]. Due to a different focus, these authors presented very little indications of metal single-atoms, not reporting e.g., EXAFS and aberration-corrected TEM.

Single-Atom heterogeneous catalysts based on M- N_x already demonstrated potential in several promising catalytic applications, among them selective oxidation of C–H bonds [1]. The introduction of functional groups in aromatics and alkanes is of paramount interest for the petrochemical industry [38]. Selective oxidation of the C–H bond can result in high-value-added carbonyl compounds, e.g., ketones, aldehydes and carboxylic acid, key intermediates in fine chemical synthesis [38,43,44]. Fe-based systems are among the most applied catalysts in this reaction due to their abundance and low cost, but also the specific reactivity of Fe with its diverse oxidation states and their possible redox transitions [45–49]. Recently, Chen et al. reported that Fe single-atoms in N-doped carbons are especially active and selective to oxidize benzene into phenol when Fe is fourfold coordinated to nitrogen (Fe- N_4C) [50]. Herein, we successfully demonstrate the application of a simple cation exchange method on ordered Na-PHI material to obtain highly active Fe- N_4 sites which are located between the heptazine rings in the PHI structure. The synthesized Fe-PHI single-atom catalysts were successfully applied in the photocatalytic oxidation of aromatic and aliphatic sp^3 C-H bonds. In the case of aliphatic hydrocarbons, oxidation could be even performed with dioxygen.

2. Experimental

2.1. Synthesis of Na-PHI

Na-PHI was prepared by the method reported by Chen et al. [40] using melamine (1 g) ground with NaCl (10 g). The reaction mixture in a porcelain crucible was heated up in an oven under constant nitrogen flow (5 L min^{-1}) to 600°C with a heating rate of $2.3^\circ\text{C min}^{-1}$, held at 600°C for 4 h, and then allowed to cool down. The crude product was removed from the crucible, washed with deionized water (1 L), isolated by filtration, and then thoroughly washed with deionized water on the filter (1 L). After that, it was dried overnight in an oven at 60°C under vacuum.

2.2. Synthesis of Fe-PHI

The Fe^{3+} ions were introduced in the PHI structure by the cation exchanged method. To synthesize the Fe-PHI (0.1%), Na-PHI (0.1 g) were added in 2 mL $FeCl_3 \cdot 6H_2O$ solution and the mix was sonicated for 30 min. The concentration of the $FeCl_3 \cdot 6H_2O$ used according to the

concentration of iron obtained in the resulting material is presented in Table S1. After that, the Fe-PHI was extensively washed with deionized water (approximately 12 mL). The photocatalysts were separated by centrifugation in a 2 mL plastic tube (11,000 rpm, for 5 min) and dried overnight in an oven at 60°C . More details about the preparation of Fe-PHI with different concentrations of iron are presented in the support information.

2.3. Characterization

The X-ray powder diffraction patterns were recorded on Bruker D8 Advance diffractometer equipped with a scintillation counter detector with $CuK\alpha$ radiation ($\lambda = 0.15418\text{ nm}$) applying 2θ step size of 0.05° and counting time of 3 s per step. Steady-state UV–vis absorption spectra were acquired using Shimadzu UV 2600 in diffuse reflectance mode. Fourier transform infrared attenuated total reflectance (FTIR-ATR) spectra were recorded on a Varian1000 FT-IR spectrometer equipped with an attenuated total reflection unit with diamond, with a resolution of 4 cm^{-1} . Elemental combustion analysis was accomplished using a Vario Micro device. Inductively coupled plasma-optical emission spectrometry (ICP-OES) was conducted using a Horiba Ultra 2 instrument equipped with photomultiplier tube detector.

Electron Paramagnetic Resonance (EPR) measurements were performed with a MiniScope X-band EPR spectrometer (MS400 Magnetech GmbH) operating at about 9.42–9.44 GHz field frequency. For samples in suspension, DMPO (2 μL) was added to a mixture of the photocatalyst in acetonitrile (0.5 mL), H_2O_2 and benzene, in the same proportion as in the photocatalytic test. For powder samples, liquid N_2 was used to maintain the temperature at 77 K. The selected conditions were: number of points: 4096, modulation amplitude: 0.15 mT, power: 10 mW, gain: 5. For the irradiation, a spot light source (200 W Hg-Xe lamp) with UV (300–450 nm) irradiation was used.

The extended X-ray absorption fine structure (EXAFS) spectroscopy data were collected at BL01C1 at Taiwan Light Source using fluorescence mode, with an average scanning time of 45 min. ARTEMIS and ATHENA software were used for data treatment and analysis. The wavelet fitting was performed using HAMA software. The detailed fitting parameters are summarized in the caption of the EXAFS fittings.

For transmission (TEM) and scanning transmission electron microscopy (STEM) observations, a suspension of the sample in ethanol was sonicated for 10 min and then drop-casted to a Cu grid with a lacey carbon support and dried for 5 min. The (S)TEM study was performed using a double Cs corrected JEOL JEM-ARM200F (S)TEM operated at 80 kV and equipped with a cold-field emission gun and a high-angle silicon drift energy dispersive X-ray (EDX) detector (solid angle up to 0.98 steradians with a detection area of 100 mm^2). Annular dark-field scanning transmission electron microscopy (ADF - STEM) images were collected at a probe convergence semi-angle of 25 mrad . The “beam shower” procedure was performed for 30 min to reduce hydrocarbon contamination during subsequent imaging at high magnification.

Raman spectra were recorded using a confocal Raman microscope alpha300 (WITec, Germany) coupled with a laser excitation at wavelength of 785 nm. The laser beam was focused through a Nikon $20\times$ microscope objective lens. The Raman spectra have been measured with an integration time of 10 s under excitation laser powers 60 mW, respectively. The spectra were acquired with a thermoelectrically cooled Andor CCD detector DU401A-BV placed behind the spectrometer UHTS 300 from WITec with a spectral resolution of 3 cm^{-1} . The Raman band of a silicon wafer at 520 cm^{-1} was used to calibrate the spectrometer. The experiments under the reaction condition were performed by dropping the bottom part of the reaction mixture (highly concentrated in catalyst) over a glass microscope slide and the analysis was carried in the same way of the Fe-PHI, as described above.

Mössbauer spectra were measured at room temperature on a Fe-PHI sample containing 0.1% ^{57}Fe before and after photooxidation of ethylbenzene in O_2 atmosphere using a standard WISSEL spectrometer with a

^{57}Co source in a rhodium matrix. About 25 mg of the sample were placed in a plexiglass sample container with a diameter of 13 mm. The isomer shifts are referred to alpha-iron. The samples analyzed by Fe^{57} Mössbauer analysis were prepared by the same method of cation exchange using Na-PHI as precursor. However, the FeCl_3 solution was prepared using metallic Fe^{57} (Sigma-aldrich) and HCl (37%). Once a 20 mM solution of FeCl_3 was obtained, the preparation procedures continued as described in the synthesis of Fe-PHI section.

The Mott-Schottky measurements were performed in a Biologic MPG-2 system using a 3 electrode set up consisting of a Pt wire working as counter electrode, an Ag/AgCl as reference electrode F-doped tin oxide (FTO) glass coated with the material as working electrode. The working electrode was prepared on FTO glass that was cleaned by sonication in ethanol for 30 min and dried at 353 K. The boundary of FTO glass was protected using Scotch tape. The 3 mg sample was dispersed in 0.2 mL of water by sonication to get a slurry mixture with 20 μL of Nafion. The slurry was spread onto pretreated FTO glass. After air-drying, the Scotch tape was removed and the working electrode was further dried at 393 K for 2 h to improve adhesion.

Cyclic voltammetry experiments were run in a Biologic MPG-2 system using a 3 electrode set up consisting of a Pt wire working as counter electrode, a Ag/AgCl as reference electrode and a 5 mm GC coated with the material as working electrode. A slurry was prepared using 3 mg sample and 20 μL of Nafion as binder in 0.2 mL of water, the mix was sonicated by 30 min. The working electrodes were prepared by drop casting 7 μL of the slurry on top of the glassy carbon electrode. Finally, the electrode was dried overnight in an oven at 60 °C. The electrolyte used was a 0.1 M 1-butyl-3-methylimidazolium tetrafluoroborate solution in CH_3CN . Previous to each experiment 25 μL of H_2SO_4 (96%) was added to the electrolyte (final concentration of 0.05 M) and oxygen was bubble for at least 10 min. Cyclic voltammograms were recorded from –0.1–1.6 V at 5 mV/s scan rate at dark and under light irradiation (410 nm).

X-ray photoelectron spectroscopy (XPS) measurements were performed on a ThermoScientific Escalab 250 Xi. A microfocused, monochromated Al K α X-ray source (1486.68 eV) and a 400 μm spot size were used in the analysis. Samples were prepared using carbon tape. LiCl was added to each sample in order to calibrate the binding energies towards Li. ThermoScientific Avantage software was used to analyze the resulting spectra.

Nitrogen adsorption and desorption isotherms were performed at 77 K in a Quantachrome Quadrasorb SI apparatus. The samples were degassed at 150 °C under vacuum (0.5 Torr) for 20 h before the measurements (3 P Instruments Masterprep degassing machine). The Brunauer–Emmett–Teller (BET) method was applied to calculate the specific surface area from adsorption branch data ($P/P_0 < 0.2$). The total pore volume (VT) was calculated from the amount of gas adsorbed at $P/P_0 = 0.995$. Pore size distributions were calculated by the nitrogen adsorption branch using the BJH model.

2.4. Photocatalytic tests

All the substrates tested here, apart from benzene, were tested adding Fe-PHI (25 or 10 mg), substrate (0.16 mmol), H_2SO_4 (0.10 mmol) and CH_3CN (2 mL). The tests under 1 bar pressure were performed in 4 mL vials connected to an O_2 balloon. The tests at 4 bar of oxygen were performed in 12 mL fisher reactors. The reactions performed under light were irradiated with a 50 W 410 nm LED lamp. After the reaction, dodecane (1 μL) was added as an internal standard. The products of the reaction were analyzed with GC-FID and GC-MS.

The benzene oxidation reaction was carried out in a 50.0 mL glass reactor with a 400 W halogen lamp as a light source. In each test, Fe-PHI (10 mg), benzene (0.1 mL), H_2O_2 (1.5 mL, 30 wt%), and CH_3CN (3 mL) were added. After the reaction, 0.75 mL of the reaction was collected after centrifugation (13,000 rpm, 3 min), dodecane (50 μL) was added as an internal standard with 1.5 mL of THF (4 °C). The products of the

reaction were analyzed with GC and GC-MS. The yield of phenol was calculated as (mole of phenol)/(mole of initial benzene) \times 100%. The selectivity of phenol was calculated as (mole of formed phenol)/(mole of formed phenol + mole of formed benzoquinone + mole of formed hydroquinone) \times 100%.

Control experiments using different radical scavengers (EDTA as a scavenger for photo-generated holes, potassium persulfate as a scavenger for electrons and *tert*-butyl alcohol as a scavenger for hydroxyl radicals) were performed under the same conditions as described above except for the addition of the radical scavengers (0.05 M in the corresponding solvent) to the reaction system.

2.5. H_2O_2 determination

The H_2O_2 produced in situ under the photocatalytic condition was quantified by the colorimetric method based on the reaction of H_2O_2 and $\text{Ti}(\text{SO}_4)_2$ in acid medium ($\text{Ti}(\text{IV}) + \text{H}_2\text{O}_2 + 2 \text{H}_2\text{O} \rightarrow \text{H}_2\text{TiO}_4 + 4 \text{H}^+$). The absorbance of the yellow-colored H_2TiO_4 at 410 nm is proportional to the reacted H_2O_2 concentration. The quantification was performed by measuring the absorbance at 410 nm (Shimadzu UV 2600) for a 0.5 mL sample, after the addition of 1.5 mL $\text{Ti}(\text{SO}_4)_2$ solution [51].

2.6. Recycling tests

The reuse of the catalyst was performed by separating the catalyst by centrifugation (13,000 rpm, 3 min) from the reaction mixture in safe lock tubes (2 mL). The catalyst was washed with methanol (2 mL), the washing was repeated three times. After that, the separated catalyst was dried at 60 °C under vacuum overnight. For the ethylbenzene photo-oxidation, the following cycles were performed under the same conditions of a typical reaction, apart from the H_2SO_4 that was adjusted to 0.04 mmol from cycle 2 and beyond.

2.7. Computational details

Spin-polarized periodic density functional theory (DFT) calculations were carried out using projector augmentation plane-wave (PAW) method [52] as implemented in the Vienna Ab initio Simulation Package (VASP) [53,54]. The PBE generalized gradient approximation to the unknown exchange-correlation functional was employed together with Grimme's empirical dispersion correction (PBE+D3) [55,56]. To represent the Kohn-Sham orbitals, the plane-wave cutoff energy was set to 350 eV and the first Brillouin zone was sampled using a $2 \times 2 \times 4$ Monkhorst-Pack k-points mesh [57]. In our calculations, the Fe-PHI model (Fe₂C₂₄N₃₄) contains two atomic layers with $a=b=12.922 \text{ \AA}$, $c=8.752 \text{ \AA}$, $\alpha = \beta = 109.6^\circ$, $\gamma = 120.35^\circ$ as lattice parameters, respectively.

The 2s2p valence states of C, 2s2p of N and 3d4s of Fe were treated explicitly in our DFT calculations. All atomic structures were optimized using the conjugate gradient algorithm till the atomic forces of all atoms turned out to be smaller than 0.01 eV, while the cell parameters were fixed to their initial values.

3. Results and discussion

3.1. Preparation of the iron single-atoms by cation exchange

The method of preparation of carbon nitride supports occurs through thermal treatment of melamine. In the case of Na-PHI, this thermal condensation takes place in the presence of sodium chloride (NaCl), producing a highly crystalline material composed of heptazine units (Fig. 1a). This process favors the reduction of defects in the structure of carbon nitride during the synthesis. The as-prepared material is labeled as Na-PHI, due to the presence of Na^+ ions between the layers of a poly (heptazine imide) motif.

Crystalline Na-PHI was then used as the scaffold for the stabilization

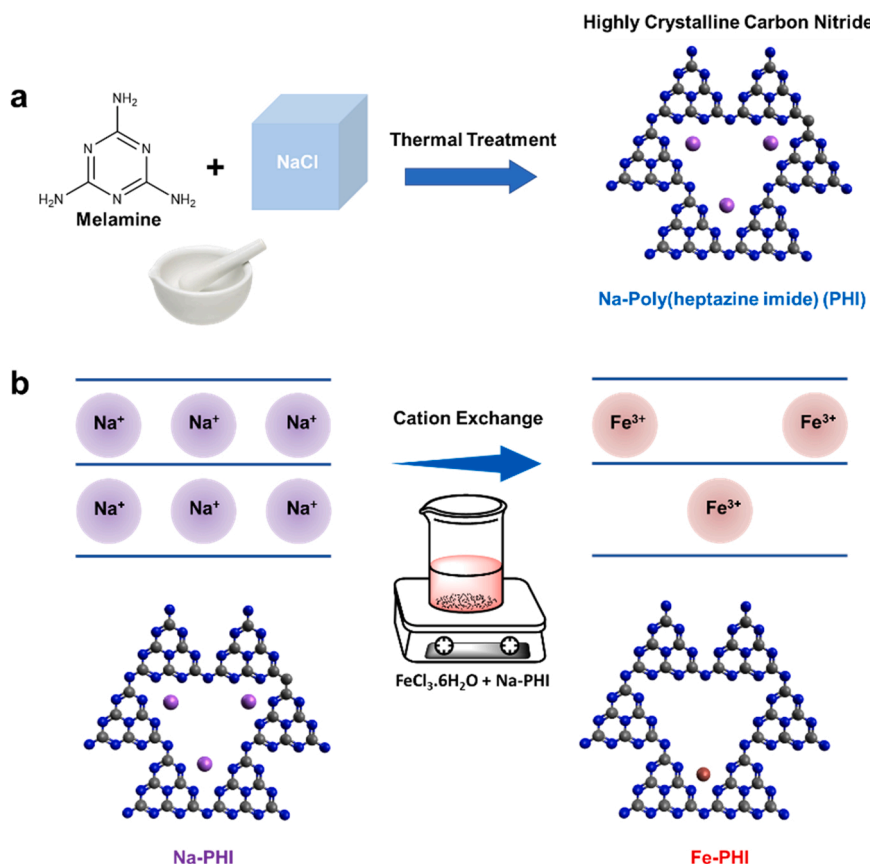


Fig. 1. (a) Schematic representation of the highly crystalline Na-PHI synthesis by the thermal condensation of melamine in the presence of NaCl; (b) Schematic representation of the controlled non-thermal cation exchange method used to replace the Na⁺ cations in the structure of PHI by Fe³⁺ cations.

of Fe atoms. The method employed is a simple cation exchange of the Na⁺ by Fe³⁺ ions, performed at room temperature. An aqueous suspension of Na-PHI and the iron precursor (a FeCl₃ solution) were mixed and stirred to produce stable Fe³⁺ in the PHI matrix. The obtained catalyst is labeled as Fe-PHI (Fig. 1b). By controlling the FeCl₃ concentration during the cation exchange it is possible to obtain a set of materials with the concentration of iron ranging from 5 to 0.02 wt%, with the remaining charges still compensated by Na-ions (Table S1).

3.2. Characterization of the Fe-PHI

The crystal structures of Na-PHI and Fe-PHI were analyzed using X-ray powder diffraction (XRD) (Fig. 2a and Fig. S2) and high-resolution transmission electron microscopy (HR-TEM) (Fig. 2b and c). HR-TEM images show that both materials form big flakes, consisting of nanometer-size crystalline domains. XRD and selected area electron diffraction patterns of both Na-PHI and Fe-PHI can be indexed in a hexagonal lattice (space group P31m). The positions of *h*00 and *h*k0 reflections in the XRD patterns are the same for both compounds, indicating that the 2D structure of PHI-layers is preserved during the ion-exchange reaction. The PHI layers are aligned directly on top of each other forming continuous channels along the *c* direction (AAA stacking) [58]. The main difference in Fe-PHI XRD peaks is observed in the range 2θ = 25–30°, indicating both a slight lattice contraction along the *c* direction, and an increasing apparent loss of regularity. As Fe is the strongest electron scatterer, this apparent disorder can be mostly related to the statistical positioning of Fe ions within the crystalline host framework. Despite neither one of the three possible positions in the unit cell nor occupation of neighboring cells is regular, the coordination environment of each iron center remains the same. The metal loading in the sample Fe-PHI was quantified by ICP-OES (Table S1). For loadings of

5 wt% Fe, contamination of FeOOH spikes becomes visible in the TEM, indicating that the iron species are no longer only single-atoms (Fig. S3a and b). EDX mapping was performed for the sample Fe-PHI-0.2% (Fig. S4) and the iron species seem to be well dispersed in the material structure. Further characterizations were performed for this same sample comparing it with the Na-PHI precursor, the results are presented and discussed in the SI. As shown in Fig. S5, the UV–vis diffuse reflectance absorption spectra (DRS) for the iron exchanged sample presents an absorption band at longer wavelengths, indicating that intraband states were introduced.

The first piece of evidence that Fe³⁺ ions are strongly coordinated by the PHI structure is obtained by comparison of the Fourier-transform infrared (FT-IR) spectra of Na-PHI and Fe-PHI (Fig. S6). Therein, a redshift of the vibrational bands related to the PHI structure after cation exchange was observed, suggesting that the metal introduced in the structure is coordinated. Furthermore, the Fe³⁺ exchange in the PHI structure is irreversible, as the Fe-PHI cannot be converted back into Na-PHI upon treatment with an aqueous solution of Na⁺ ions. This fact indicates that once the Fe³⁺ ions exchange the Na⁺ ions they form strong bonds with the PHI structure. The extended X-ray absorption fine structure (EXAFS) Fourier transforms (FTs) and wavelet transforms (WTs) are shown in (Fig. 3a–c). The detailed analysis suggests that once the Fe³⁺ are exchanged in the PHI structure, they bind with the N atoms of the heptazine rings. Spin-polarized periodic density functional theory (DFT) calculations give more details on the energetically favored atomic structure of Fe-PHI. The cations in the PHI-scaffold could either be located in the plane of PHI-layers or between them [59]. Our DFT simulations suggest that the Fe³⁺ ions are located between the PHI-layers. The Fe³⁺ ions are coordinated to four N atoms, two from each PHI-layers (Fig. 3d), a favorable geometry to support catalysis. The Bader charge analysis further shed light on the interaction between Fe

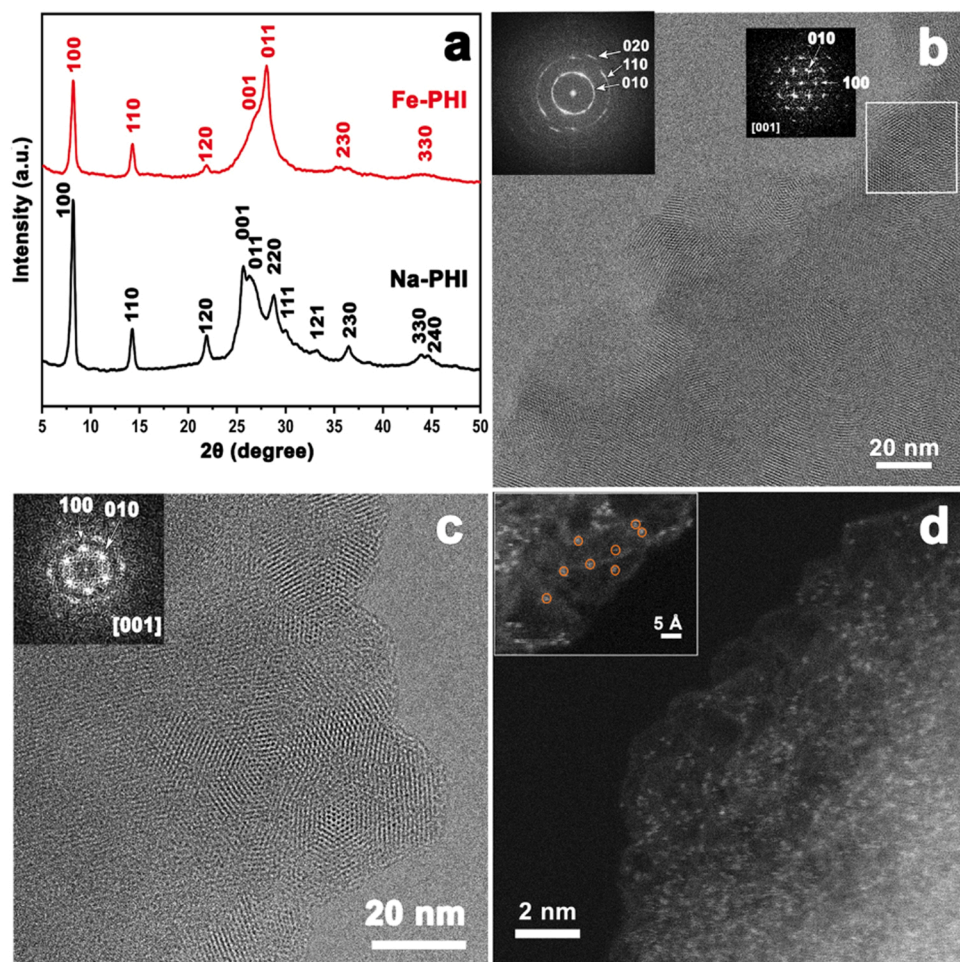


Fig. 2. (a) Powder XRD patterns for Na-PHI and Na-PHI exchanged by Fe^{3+} (Fe-PHI) with 0.1% Fe^{3+} ; (b) HR-TEM image of a typical Na-PHI flake showing crystalline nanodomains; the corresponding fast Fourier transformation (FFT) is given in the inset (left). The white square shows the approximate area of the individual grain and the corresponding FFT pattern (inset on the right), which is indexed in a hexagonal lattice. (c) HR-TEM image of Fe-PHI (0.1%) and the corresponding FFT (left) indexed in a hexagonal lattice; (d) Annular dark-field scanning transmission electron microscopy image of Fe-PHI showing metal single-atoms.

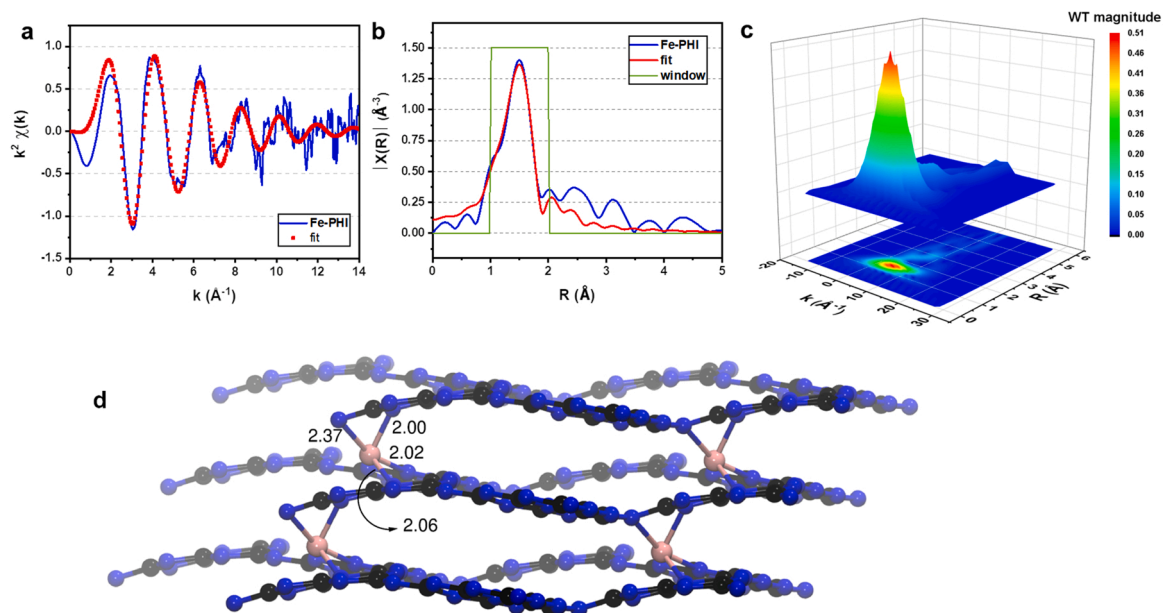


Fig. 3. (a) Fe K-edge EXAFS (line) and curve fit (points) for Fe-PHI, shown in k_2 weighted k -space. (b) Fe K-edge EXAFS (blue) and curve fit (red) for Fe-PHI, shown in k_2 weighted R -space. (c) Wavelet transform for k_2 weighted EXAFS signal; (d) The atomic structure of Fe-PHI obtained from spin-polarized DFT simulation. The distances between Fe and nearest N atoms are marked in \AA units. Atoms color: C-black, N-blue and Fe-pink.

and PHI-scaffold, as shown in Fig. S27. The charge analysis clearly indicates that the PHI-layer is negatively charged, which is compensated by the positively charged Fe atoms.

Aberration-corrected high-angle annular dark-field scanning transmission electron microscopy (AC-HAADF-STEM) confirms the presence of single-atoms in Fe-PHI as presented in Fig. 2d. The coordination environment of the iron atoms can also be revealed. To better correlate the EXAFS peaks with k-space, wavelet transformation (WT) was employed (Fig. 3a). The highest intensity belongs to the lobe centered at $k = 6 \text{ \AA}^{-1}$, $R = 1.5 \text{ \AA}$, which can correspond to possible O or N atoms around the Fe center, with very weak back-scattering and the absence of long-range Fe-Fe scattering paths at higher radial distances (at $k > 10 \text{ \AA}^{-1}$, $R > 2.5 \text{ \AA}$). The latter point indicates the absence of direct Fe-Fe interaction [60]. The coordination information of the Fe centers is obtained by the fitting of the EXAFS data (k-space in Fig. 3b and R-space in Fig. 3c). The first peak corresponds to Fe-N(C) contribution with a fitted bond length of $2.02(1) \text{ \AA}$, which is attributed to the first shell coordination of Fe-N (Fig. S7). The coordination number of Fe is determined as 4.8(5), which is in agreement with the structure optimized by DFT (Fig. 3d). As the EXAFS does not allow differentiating between Fe-O and Fe-N bonds, the existence of Fe-O bonds due to water in the pores cannot be excluded. However, a coordination number of 4.8 for the iron centers is more suitable for the formation/stabilization of the later discussed active sites, e.g., $\text{Fe}=\text{O}$ and $\text{O}=\text{Fe}=\text{O}$, which are formed in the presence of H_2O_2 and light. The formation of these species will be further discussed in the mechanism section.

3.3. Photooxidation of sp^3 C-H bonds

The high dissociation energy of the C-H bond and the ease of possible over-oxidation occurring as side reactions (products are more easily oxidized than the educts) make the selective direct oxidation of C-H bonds very challenging. Fe single-atoms-based catalysts with a high oxidation state of the iron centers are a promising option to promote the selective oxidation of hydrocarbons. However, stronger oxidants than O_2 , such as H_2O_2 and *tert*-butyl hydroperoxide, are mostly added in the reaction to promote the formation of a highly oxidized iron species (i.e., Fe^{IV}) [38,50].

Herein, we apply Fe-PHI SACs to catalyze the photooxidation of aliphatic hydrocarbons using only O_2 . Ethylbenzene was used as a model substrate to investigate the oxygen insertion reaction. Interestingly, Fe-PHI (0.1%) possesses the most active iron centers (Fig. 4c), leading to a 99.6% conversion of ethylbenzene at a 98.4% selectivity toward

Table 1

Conversion, selectivity and TOF for the photocatalytic transformation of ethylbenzene into acetophenone.

Entry	Catalyst	Conv. (%)	Selec. (%)	TOF (h^{-1})
1	Fe-PHI (0.1%)	99.6	98.4	65.8
2 ^{a,b}	Fe-PHI (0.1%)	6.0	78.3	0.4×10^{-3}
3 ^a	Fe-PHI (0.1%)	0.0	0.0	0.0
4 ^b	Fe-PHI (0.1%)	92.7	95.1	7.7
5 ^{b,c}	FeCl_3	11.9	27.3	0.12
6	Na-PHI	14.4	50.8	–

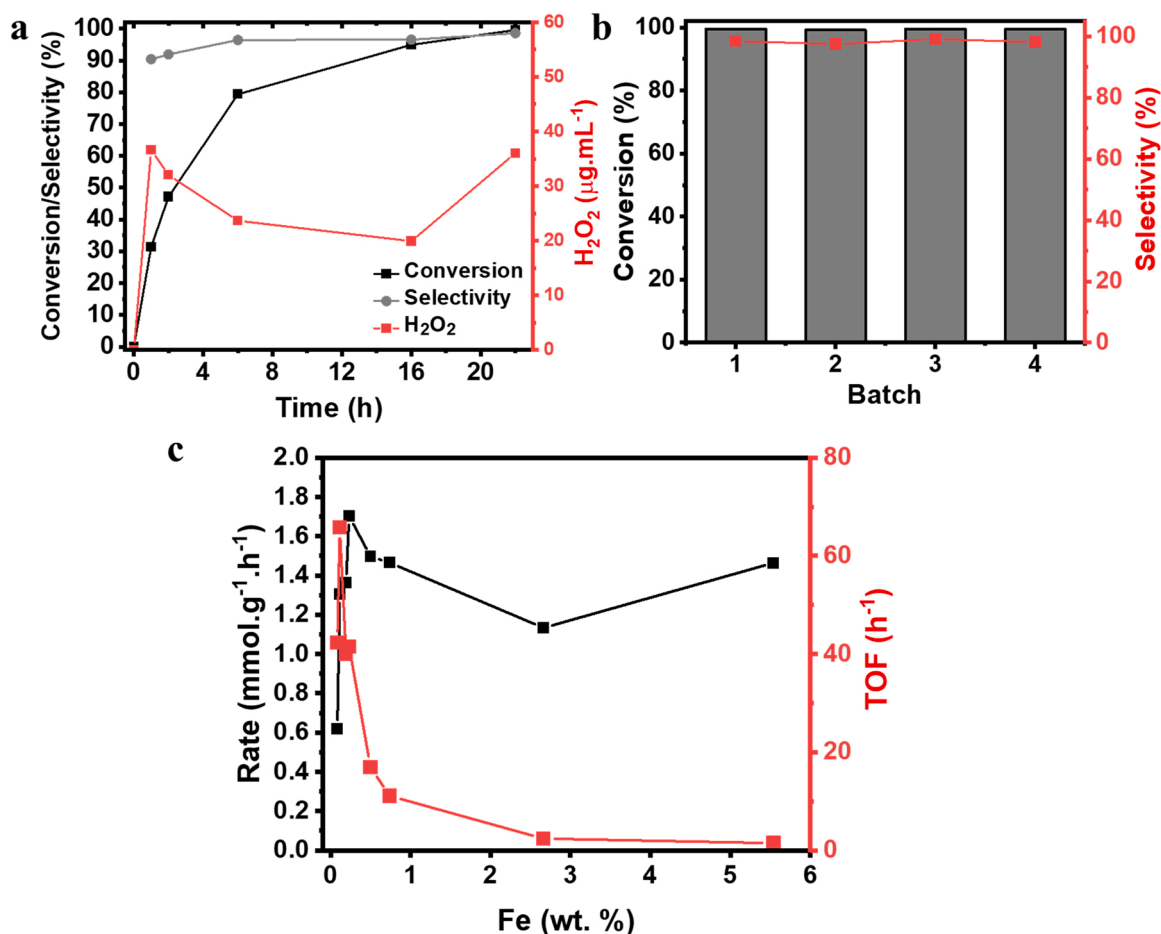


Fig. 4. (a) Kinetics for the photooxidation of ethylbenzene into acetophenone catalyzed by Fe-PHI (0.1%); (b) Conversion and selectivity for the ethylbenzene photooxidation performed by different batches of Fe-PHI (0.1%), demonstrating the high reproducibility of the SAC; (c) Rate and TOF for Fe-PHI with different iron loadings.

acetophenone (Table 1, Entry 1). The reaction takes place relatively fast and displays 80% conversion within 6 h (Fig. 4a).

Even if only O₂ is added as oxidant, H₂O₂ is produced in situ by the Fe-PHI catalyst under light irradiation, as demonstrated by the quantification of H₂O₂ in the medium during the reaction kinetics (Fig. 4a). As shown in Fig. 4a, in the first hour of reaction, H₂O₂ concentration is rapidly increasing, but also progressively consumed during the reaction. The reaction using only O₂ as oxidant (Entry 1) displaying a performance even better than the Fe-PHI (0.1%) in the presence of H₂O₂ (Entry 4), suggesting that the formation of H₂O₂ in situ increments the catalyst activity and improves its selectivity.

Reaction conditions: catalyst (25 mg), ethylbenzene (20 µL, 0.16 mmol), H₂SO₄ (5 µL, 0.1 mmol), 1 bar O₂, r.t., 22 h, 50 W 410 nm LED. ^aNo light; ^b H₂O₂ (60 µL, 50 wt%, 2.5 mmol); ^c0.04 mmol FeCl₃. Products were quantified by GC-FID analysis with dodecane as an internal standard.

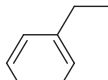
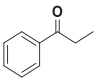
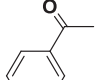
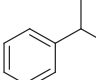
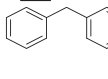
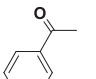
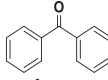
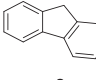
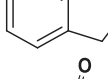
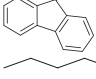
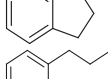
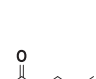
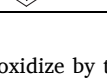
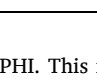
A set of control experiments were performed to confirm that the reaction occurs through a photo-promoted mechanism catalyzed by the heterogeneous Fe-PHI catalyst. Firstly, the reaction was tested in the dark with the addition of H₂O₂, since it is well known that the H₂O₂ production by carbon nitride-based materials depends on light irradiation [61]. Without light irradiation and with the addition of 2.5 mmol of H₂O₂ the ethylbenzene conversion drops to 6.0% (Entry 2), indicating that light is essential not only for the H₂O₂ formation in-situ, but also for the promotion of the active site. Without light and H₂O₂, negligible amount of products are detected (Entry 3). In order to investigate the possibility of the reaction to take place through a homogenous Fenton-like mechanism, the reaction was performed by adding FeCl₃ (Entry 5) in the same concentration range of iron in the Fe-PHI sample (0.04 mmol). The conversion and selectivity for acetophenone massively decreased in comparison to Fe-PHI, indicating that the reaction takes place through a heterogeneous mechanism and not by a homogeneous mechanism promoted by potentially leached Fe ions. This was also confirmed by ICP-OES analysis of the reaction medium, which indicates a negligible amount of iron ions in the solution. The Fe-PHI precursor (i.e., Na-PHI) was also tested in the reaction (Entry 6). It shows a significantly poorer activity compared with Fe-PHI (Entry 1), in agreement with the previously reported fact that carbon nitride is capable to promote the oxidation of ethylbenzene [62].

In order to confirm the reproducibility of the cation exchange method to obtain active iron SACs, four Fe-PHI (0.1%) samples were synthesized in different batches by the same method (Fig. 4b). All the samples displayed high activity for the photooxidation of ethylbenzene into acetophenone, presenting conversions higher than 99% and selectivity higher than 97.5%, and the cation exchanged method presented in this work has shown excellent reproducibility and reliability. One of the advantages of the cation exchange method in the preparation of SACs is the fine control of the Fe content in the samples. For example, applying the cation exchange method it was possible to evaluate the iron center activity in function of the iron concentration, Fe-PHI samples with different loading of Fe were tested. Fig. 4c shows that the activity per iron center (TOF) greatly increases for the samples with loadings lower than 1%, reaching an optimum point at 0.1%. The overall activity (rate) also presents a maximum close to 0.1% and seems to reach a plateau at concentrations higher than 1%. As their characterization indicates, samples with higher loading of iron seem to be a mix of single-atoms with larger iron oxide structures. Once these other iron species are significantly less active for the C-H bond oxidation, they will necessarily display a lower activity per iron content (TOF) and no increment in the rate.

The remarkable activity presented by the Fe-PHI SACs in the photooxidation of ethylbenzene motivated us to test it for a broader scope of substrates. As shown in Table 2, high conversion and selectivity to ketones were achieved in the case of secondary benzylic carbons, such as diphenylmethane (Entry 2), indan (Entry 3) and propylbenzene (Entry 4). Bulkier substrates, such as fluorene (Entry 6) seem to be

Table 2

Conversion and selectivity for hydrocarbons photooxidation.

Entry	Substrate	Product	Conv. (%)	Selec. (%)
1			99.7	98.6
2			99.8	100
3			100	94.5
4			94.8	87.5
5			88.8	96.2
6			46.9	100
7			72.6	100

harder to oxidize by the Fe-PHI. This is expected once the active iron centers are localized between the PHI layers deep in the bulk of the material. Curiously, tertiary carbons, such as cumene (Entry 5), lead to acetophenone and not alcohol as other SACs previously reported, [38] indicating that the Fe-mechanism of PHI under oxygen tends to be very selective to ketones, even if it includes C-C splitting. The Fe-PHI stability was evaluated by testing its reuse in consecutive cycles. As shown in Fig. S8, it preserves most of its activity over the reuse cycles, displaying 96% conversion and 96% selectivity after 4 cycles. Characterizations were performed for the samples before and after the reaction, the results are presented in discussed in the SI.

Reaction conditions: Fe-PHI (0.1%) (25 mg), substrate (0.16 mmol), H₂SO₄ (5 µL, 0.1 mmol), 4 bar O₂, r.t., 22 h, 50 W 410 nm LED. Conversion and selectivity were determined by GC-MS and GC-FID analysis with dodecane as an internal standard.

Tests with scavengers were performed to get insights about the reaction mechanism and the role of each component in the reaction. As shown in Fig. S9, the addition of K₂S₂O₈ (electron scavenger) strongly affect the catalyst activity, due to the suppression of the H₂O₂ production, which depends on electrons [61]. This was confirmed by the addition of H₂O₂ in the test with K₂S₂O₈, as presented in Fig. S8, where the Fe-PHI activity is completely restored. On the other hand, the addition of EDTA (hole scavenger) decreased the TOF of Fe-PHI by 60% (Fig. S8), indicating that holes have an important role in the reaction; This will be further discussed in the mechanism section. The addition of *tert*-butanol and methanol, a hydroxyl radical scavenger and a sulfate radical scavenger [63], respectively, did not cause a significant change in Fe-PHI activity, suggesting that hydroxyl radicals and sulfate radicals are not involved in the reaction mechanism, i.e., it is not a Fenton mechanism (Fig. S8).

3.4. Photooxidation of benzene

The oxidation of an aromatic C-H bond to phenols is the next higher target of catalytic oxidation [46,64–66]. The industrial production of phenol is currently based on the rather inefficient three-step cumene process, which comes with lower yields, high energy consumption, and a hazardous cumene hydroperoxide intermediate [64,65]. The development of an one-step selective oxidation of benzene to phenol is of

paramount importance, and several reports employed different conditions, catalysts, and reagents (O_2 , H_2O_2) to drive this reaction [46,49,64,65,67–70]. Given the excellent performance displayed by Fe-PHI SACs for the C-H bonds oxidation reactions, Fe-PHI SACs were also tested in the direct photocatalytic conversion of benzene into phenol (Table 3). The Fe-PHI indeed showed a benzene conversion of 45.5% and 98.5% selectivity toward phenol (Table 3, Entry 1). Different from the insertion of oxygen in C-H aliphatic (sp^3 carbon), the oxidation of a C-H aryl carbon (sp^2) was only successful with the addition of H_2O_2 . These results were obtained using H_2SO_4 as a promoter (Fig. S10), suggesting that the reaction is favored in acid conditions. Yield can be further improved by increasing the reaction time (Fig. S11). Doubling reaction time gave phenol with 61% yield and 98.8% selectivity (Entry 3). The influence of free Fe^{3+} ions in the reaction medium was investigated testing the reaction under the same condition using a solution of $FeCl_3$ as catalyst (Entry 6). The conversion and selectivity for phenol decreased in comparison to Fe-PHI, indicating that the reaction takes place through a heterogeneous mechanism and not homogeneously by potentially leached Fe ions. Also, different catalysts were tested in the reaction. All of them showed conversion and selectivity significantly lower compared to Fe-PHI SACs, demonstrating that single-atom Fe-PHI-based catalysts are highly effective in the photocatalytic oxidation of benzene to phenol (Fig. S12).

Reaction conditions: catalyst (10 mg), benzene (100 μ L, 1.1 mmol), H_2O_2 (1.5 mL, 30 wt%, 15 mmol), H_2SO_4 (10 μ L, 0.2 mmol), 60 °C, 400 W halogen lamp. ^a H_2SO_4 (20 μ L, 0.4 mmol); ^bNo light; ^c0.08 mol $FeCl_3$.

In order to verify the photooxidation mode, a set of control experiments without light was performed (Fig. S13b). The results showed a conversion of 2.5% with a selectivity of 85% (Entry 5), confirming that photocatalytic activation increases the reaction yield. The use of hydrogen peroxide and acetonitrile is essential for the control of conversion and selectivity of the reaction. Thus, performing the reaction using only water and peroxide led to the formation of a large number of unidentified products that formed presumably via oxidative phenol or intermediate coupling. A lower amount of hydrogen peroxide decreased the yield of phenol. Furthermore, changing the concentration of hydrogen peroxide (from 30% to 50%) did not influence the conversion (Fig. S13a). The presence of H_2SO_4 in the reaction at the concentrations tested here did not significantly affect the stability of the Fe-PHI SAC, as shown by the recycling experiments, where the conversion of benzene remained at 39.5% without loss of selectivity for phenol. After three reuses, the benzene conversion falls by 12%, showing that even after several reactions the catalyst is still active and selective (Fig. S13d).

3.5. Mechanism investigation

Catalytic studies with scavengers were performed to understand the reaction mechanism. As shown in Fig. S14, the addition of *tert*-butanol, a hydroxyl radical scavenger, did not cause any change in conversion/selectivity, suggesting that hydroxyl radicals are not involved in the reaction mechanism. This was also confirmed by EPR experiments (Fig. S15). Therefore, we can state that the reaction does not take place via a classical Fenton or photo-Fenton mechanism. Electron scavenger also does not seem to affect the photocatalyst activity (Fig. S14 and S9). On the other hand, the addition of EDTA (a hole scavenger) decreased

the TOF of Fe-PHI (Fig. S14 and S9). Thus, we conclude that the oxidation reaction is promoted by holes, possibly by their transfer to iron centers. We believe that the reaction occurs through the C-H activation mechanism catalyzed by iron-oxo species similar to the mechanism reported by Chen et al. [50]. However, in our case the iron-oxo species are photo promoted, accelerating their formation by employing the extra energy of 2.8 eV (Fig. 5a). This is confirmed by the EPR data (Fig. 5b) for the Fe-PHI SACs under the reaction conditions after some minutes of irradiation, in which a shoulder arises in the spectrum close to the region g factor of 2.00, where also the delocalized electrons in the π -conjugated structure of the PHI are observed (Fig. S16a). We attribute this shoulder to a dioxo-Fe(V) species, [71] which would be formed by the further oxidation of the iron centers by localization of the photogenerated holes. The presence of iron-oxo species was also confirmed by Raman spectroscopy (Fig. 5c), which displays a shoulder at 808 cm^{-1} typical of iron-oxo ($Fe=O$) bonds [71,72]. The formation of Fe(IV) and Fe(V) species can in addition be evidenced by cyclic voltammetry (Fig. S17), where two redox features at 0.8 V and 1.2 V appear. These are usually attributed to the formation of Fe(IV) and Fe(V) species, respectively [73]. It is worth noting that after illumination the peak at 1.2 V assigned to Fe(V) increases, corroborating with the EPR analysis, which suggests the generation of Fe(V) species under light irradiation.

The Mössbauer spectrum collected for the Fe-PHI sample containing 0.1% ^{57}Fe before the reaction shows two doublets (Fig. 6) with nearly identical isomer shift (IS), but different quadrupole splitting (QS). This indicates two somewhat different coordination environments but with similar chemical bonding. The Mössbauer parameters (Table 4) are compatible with Fe(III) high spin sites in five- or six-fold coordination geometry, in agreement with our EXAFS, EPR results and theoretical simulation that indicate Fe(III) tetracoordinated to nitrogen between the PHI layers and a total coordination number of 4.8. Similar results were reported by for Fe(III) single-atoms stabilized in N-doped carbons. After photooxidation reaction with O_2 , the Mössbauer spectrum exhibits only one broadened singlet with an enhanced isomer shift. The IS and QS values are compatible with Fe(II) low spin or Fe(III) high spin in a quite regular coordination environment (small QS). Similar to other works on single-atom based materials [50], the Mössbauer spectra do not show evidence for the presence of Fe(IV) or Fe(V) which would give rise to a considerably smaller IS. This can be due to the fact that the Mössbauer analysis cannot be performed under reaction conditions, and the Fe(IV) and Fe(V) do not seem to be stable outside the reaction medium. These species were in fact never detected by Mössbauer analysis before for single-atom based materials. The obtained spectrum may correspond to a Fe(III)-oxo or hydroxo PHI species formed by reduction of the corresponding Fe(IV)-oxo species. Closely related Fe(III)-O and Fe(IV)-O complexes with FeN_4 coordination are known to exist [74].

The reaction mechanism for the benzene oxidation proposed by Chen and collaborators starts with the H_2O_2 approaching the metal center, which oxidizes the former Fe(III) single-atom sites to the active intermediate Fe(IV)=O (Fig. 5d) [50]. This $2e^-$ process leads to oxo species, which are stable in the acidic environment, explaining the role of sulfuric acid in the reaction. [75] We assume that this site can react with another H_2O_2 molecule, under light irradiation, via another two-electron oxidation to give a Fe(V)-dioxo-species, which of course is, even more, oxidative (Fig. 5d). The oxidation of the metal center is presumably promoted by the light-driven pathway, due to the highly positive position of the VB (+2.8 V vs RHE, Fig. S18), where the photogenerated holes have more than enough oxidation power to oxidize Fe(III) into Fe(IV)/Fe(V) species (Fig. 5a).⁶¹ The light-separated electrons stay delocalized in the π -conjugated structure to compensate the positive charge of Fe(V) species, as evidenced by the rather strong ESR signal with the g factor of 2.00 (Fig. 5b). This signal increases with irradiation time. In any case, the strongly oxidizing hole facilitates the oxidation of iron and the formation of iron species in both oxidation stages (steps 2 and 3 Fig. 5d). The higher TOFs reported here are only found under light

Table 3
Conversion and selectivity for the direct transformation of benzene into phenol.

Entry	Catalyst	Time (h)	Conv. (%)	Selec. (%)
1	Fe-PHI	22	45.5	98.5
2 ^a	Fe-PHI	22	40.2	96.9
3	Fe-PHI	44	60.9	98.8
4	–	22	0.5	63.2
5 ^b	Fe-PHI	22	2.5	84.9
6 ^c	$FeCl_3$	22	0.6	73

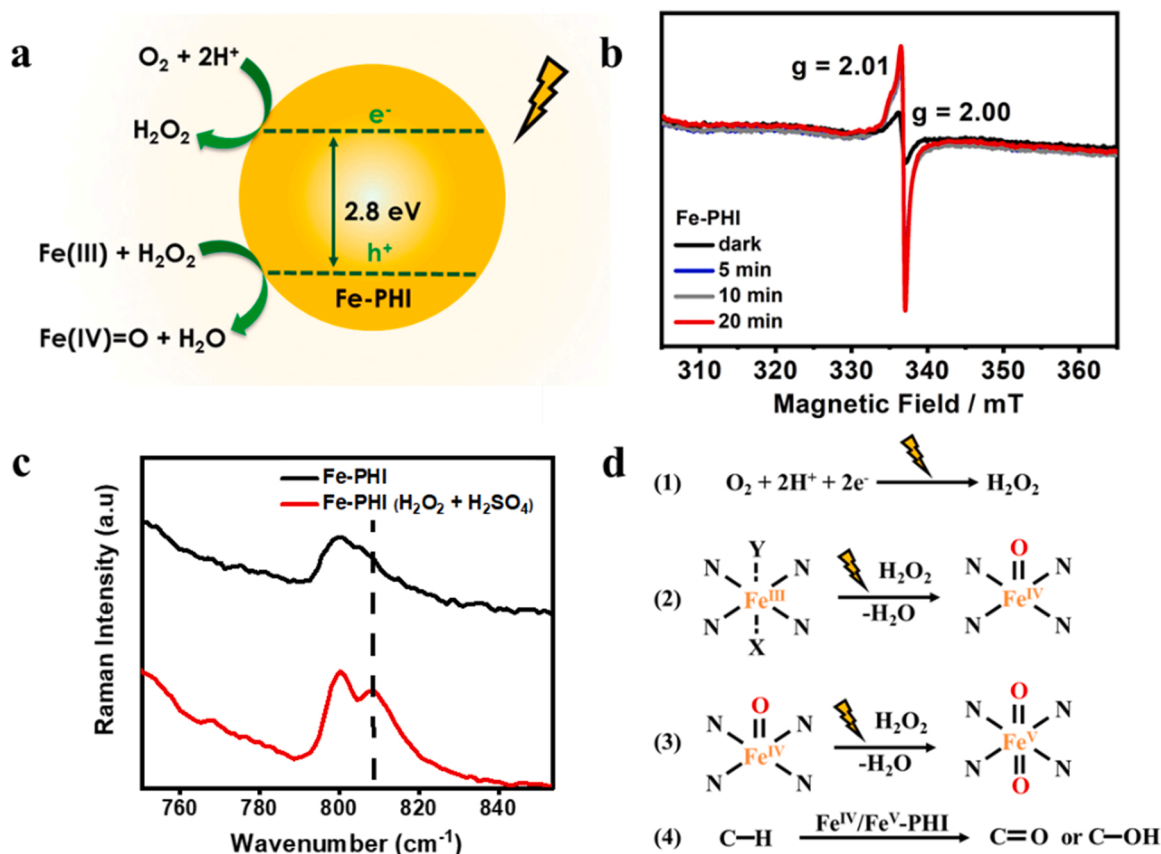


Fig. 5. (a) Schematic representation of the e^-/h^+ separation promoting effect on the formation of active high oxidation state iron centers; (b) EPR spectra of Fe-PHI in the dark and under irradiation for different time intervals in the reaction conditions Fe-PHI (before and after reaction) acquired in solid-state; (c) Resonance Raman spectra of Fe-PHI and Fe-PHI in the presence of H_2O_2 and H_2SO_4 collected using 785 nm laser; (d) Proposed mechanism of formation of the active Fe(IV)/Fe(V) sites.

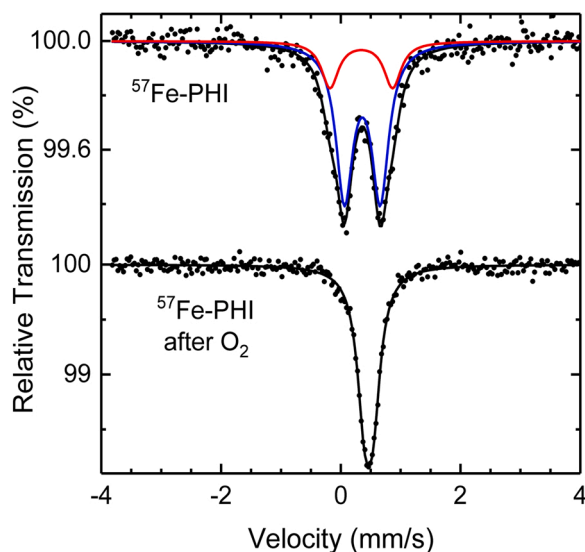


Fig. 6. ^{57}Fe Mössbauer spectra at room temperature for Fe-PHI and Fe-PHI after the photooxidation reaction with O_2 . The samples contained 0.1% ^{57}Fe .

irradiation, which underlines the role of PHI as the sensitizer to lift the oxidation power of the system by employing the energy of photons. Next, the benzene C-H bond is activated through the oxygen rebound mechanism (step 4 Fig. 5d), which is well-known from Cytochrome P450 (Fig. S19) [76]. The mechanisms for aliphatic and aromatic C-H

Table 4

^{57}Fe Mössbauer parameters of Fe-PHI and Fe-PHI after the photooxidation reaction with O_2 .

IS ($mm\ s^{-1}$)	QS ($mm\ s^{-1}$)	Γ ($mm\ s^{-1}$)	Area (%)
0.359(3)	0.597(12)	0.34(1)	77
0.342(10)	1.05(3)	0.34 *	23
0.466(2)	0.141(8)	0.31(1)	100

oxidation should be very similar, except for the in-situ H_2O_2 production when O_2 is used as an oxidant (step 1, Fig. 5d).

4. Conclusions

In summary, we have shown a reliable and easily reproducible method to obtain highly active Fe SACs with “Fe- N_4 ” sites using a one-step simple cation exchange method. By exchanging sodium cations in high crystalline Na-PHI by Fe(III), stable Fe single-atoms located between the heptazine rings of the PHI structure were obtained. The Fe-PHI single-atom catalyst displays high selectivity and good conversions in C-H bond oxidation reactions, comparable to the best SACs based on N-rich materials reported in literature so far. The photooxidations of aliphatic C-H for different substrates were performed using only oxygen as oxidant. Furthermore, we also demonstrated that the more challenging benzene oxidation can be also catalyzed by the Fe-PHI with fair yields. The reaction mechanism was investigated in detail, indicating the participation of the support PHI in the promotion of Fe(IV)/Fe(V) species via localization of the strongly oxidizing hole photo-

generated in its band structure.

Supplemental Information

Synthesis and Characterization procedures; Computational Detailed discussion; Elemental composition data; EXAFS details; EDX mapping; FTIR investigations; UV-Vis spectroscopy data; Performance of the photocatalyst in the oxidation of benzene to phenol using different acids; Reaction kinetics; Performance of different catalysts in photocatalytic oxidation of benzene to phenol; Performance of photocatalytic oxidation of benzene to phenol at different conditions; Photocatalytic investigations with scavengers; EPR data and detailed discussion; XRD for different iron loading samples; XPS spectra for the sample before and after reaction; Pictures of the setups used in the photocatalytic oxidation reactions.

CRedit authorship contribution statement

IFT conceived and coordinated all stages of this research in collaboration with MA. IFT, IFS and MARS prepared the catalyst. IFT, MARS, NLS, NDT, BNN, DWB, QX and BTWO characterized the catalysts. PA collected and analysed the Mössbauer spectra. MARS and IFS undertook the catalytic tests. SKS and TDK conducted the computational studies. NDT conducted the AC-STEM analysis. QX and BTWO performed EXAFS investigations. BNN and DWB conducted the EPR experiments. IFT, MARS, AS, MA, NDT, BTWO, CR, SKS and TDK co-wrote the manuscript in discussion with other co-authors. Dr. Johannes Schmidt is greatly acknowledge for his support with XPS analysis.

Declaration of Competing Interest

The authors declare that they have no known competing financial interests or personal relationships that could have appeared to influence the work reported in this paper.

Acknowledgments

I.F.T thanks the Alexander von Humboldt Foundation for his post-doctoral fellowship. SKS and TDK acknowledge the generous allocation of computing time by the Paderborn Center for Parallel Computing (PC2) on OCuLUS and the FPGA-based supercomputer NOCTUA. CR and IFT acknowledges CAPES/Alexander von Humboldt Foundation for Experienced Researchers Fellowship : Coordenação de Aperfeiçoamento de Pessoal de Nível Superior-CAPES (88881.145566/2017-1 and 88881.368085/2019-01) and Return Fellowship. This research was supported financially by the Max Planck Society. The authors IFT, MARS and CR are grateful to the Brazilian funding agencies Coordenação de Aperfeiçoamento de Pessoal de Nível Superior-CAPES, Conselho Nacional de Desenvolvimento Científico e Tecnológico-CNPq (423196/2018-9) and Fundação de Amparo à Pesquisa do Estado de São Paulo-FAPESP (2020/14741-6; 2018/012585 and 2021/11162-8) for financial support. BNN gratefully acknowledges the financial support from Coordenação de Aperfeiçoamento de Pessoal de Nível Superior-CAPES, Brazil, from the CAPES/DAAD/CNPQ (15/2017) program, grant number 88887.161403/2017-00. The studies performed in the laboratory “Photoactive nanocompositematerials” were supported by Saint-Petersburg State University (ID:73032813).

Appendix A. Supporting information

Supplementary data associated with this article can be found in the online version at [doi:10.1016/j.apcatb.2021.120965](https://doi.org/10.1016/j.apcatb.2021.120965).

References

- [1] S.K. Kaiser, et al., Single-atom catalysts across the periodic table, *Chem. Rev.* 120 (21) (2020) 11703–11809.
- [2] X. Li, et al., In situ/operando techniques for characterization of single-atom catalysts, *ACS Catal.* 9 (3) (2019) 2521–2531.
- [3] B. Qiao, et al., Single-atom catalysis of CO oxidation using Pt 1/FeO x, *Nat. Chem.* 3 (8) (2011) 634–641.
- [4] A. Wang, J. Li, T. Zhang, Heterogeneous single-atom catalysis, *Nat. Rev. Chem.* 2 (6) (2018) 65–81.
- [5] L. Zhang, et al., Single-atom catalyst: a rising star for green synthesis of fine chemicals, *Natl. Sci. Rev.* 5 (5) (2018) 653–672.
- [6] S. Mitchell, E. Vorobyeva, J. Pérez-Ramírez, The multifaceted reactivity of single-atom heterogeneous catalysts, *Angew. Chem. Int. Ed.* 57 (47) (2018) 15316–15329.
- [7] C. Mondelli, et al., Biomass valorisation over metal-based solid catalysts from nanoparticles to single atoms, *Chem. Soc. Rev.* 49 (2020) 3764–3782.
- [8] M. Moliner, et al., Reversible transformation of Pt nanoparticles into single atoms inside high-silica chabazite zeolite, *J. Am. Chem. Soc.* 138 (48) (2016) 15743–15750.
- [9] Y. Liu, et al., A general strategy for fabricating isolated single metal atomic site catalysts in Y zeolite, *J. Am. Chem. Soc.* 141 (23) (2019) 9305–9311.
- [10] K. Jiang, et al., Isolated Ni single atoms in graphene nanosheets for high-performance CO2 reduction, *Energy Environ. Sci.* 11 (4) (2018) 893–903.
- [11] B.T.W. Lo, L. Ye, S.C.E. Tsang, The contribution of synchrotron X-ray powder diffraction to modern zeolite applications: a mini-review and prospects, *Chem* 4 (8) (2018) 1778–1808.
- [12] W.-C. Lin, et al., Cooperative catalytically active sites for methanol activation by single metal ion-doped H-ZSM-5, *Chem. Sci.* 12 (2020) 210–219.
- [13] L. Zhang, et al., Single atoms on graphene for energy storage and conversion, *Small Methods* 3 (9) (2019) 1800443.
- [14] Y. Wang, et al., Co single-atoms on ultrathin N-doped porous carbon via a biomass complexation strategy for high performance metal–air batteries, *J. Mater. Chem. A* 8 (4) (2020) 2131–2139.
- [15] X. Hu, et al., Ru single atoms on N-doped carbon by spatial confinement and ionic substitution strategies for high-performance Li–O2 batteries, *J. Am. Chem. Soc.* 142 (39) (2020) 16776–16786.
- [16] J.-F. Sun, et al., Isolated single atoms anchored on N-doped carbon materials as a highly efficient catalyst for electrochemical and organic reactions, *ACS Sustain. Chem. Eng.* 8 (39) (2020) 14630–14656.
- [17] Y. Meng, et al., Fluorination-assisted preparation of self-supporting single-atom Fe-N-doped single-wall carbon nanotube film as bifunctional oxygen electrode for rechargeable Zn-Air batteries, *Appl. Catal. B: Environ.* 294 (2021), 120239.
- [18] A. Han, et al., Recent advances for MOF-derived carbon-supported single-atom catalysts, *Small Methods* 3 (9) (2019) 1800471.
- [19] X. Wang, et al., 2D MOF induced accessible and exclusive Co single sites for an efficient O-silylation of alcohols with silanes, *Chem. Commun.* 55 (46) (2019) 6563–6566.
- [20] Q. Zuo, et al., Ultrathin metal–organic framework nanosheets with ultrahigh loading of single Pt atoms for efficient visible-light-driven photocatalytic H2 evolution, *Angew. Chem.* 131 (30) (2019) 10304–10309.
- [21] Q. Xue, et al., A rational study on the geometric and electronic properties of single-atom catalysts for enhanced catalytic performance, *Nanoscale* (2020).
- [22] Z. Chen, et al., Stabilization of single metal atoms on graphitic carbon nitride, *Adv. Funct. Mater.* 27 (8) (2017) 1605785.
- [23] Z. Chen, et al., A heterogeneous single-atom palladium catalyst surpassing homogeneous systems for Suzuki coupling, *Nat. Nanotechnol.* 13 (8) (2018) 702–707.
- [24] Z. Chen, et al., Single-atom heterogeneous catalysts based on distinct carbon nitride scaffolds, *Natl. Sci. Rev.* 5 (5) (2018) 642–652.
- [25] I.F. Teixeira, et al., Carbon nitrides and metal nanoparticles: from controlled synthesis to design principles for improved photocatalysis, *Chem. Soc. Rev.* 47 (20) (2018) 7783–7817.
- [26] J. Liu, et al., Ligand–metal charge transfer induced via adjustment of textural properties controls the performance of single-atom catalysts during photocatalytic degradation, *ACS Appl. Mater. Interfaces* 13 (22) (2021) 25858–25867.
- [27] D. Liu, et al., Single noble metal atoms doped 2D materials for catalysis, *Appl. Catal. B: Environ.* 297 (2021), 120389.
- [28] G. Liu, et al., Confining single-atom Pd on g-C3N4 with carbon vacancies towards enhanced photocatalytic NO conversion, *Appl. Catal. B: Environ.* 284 (2021), 119683.
- [29] X. Zhao, et al., Single-atom Co embedded in BCN matrix to achieve 100% conversion of peroxydisulfate into singlet oxygen, *Appl. Catal. B: Environ.* (2021), 120759.
- [30] C.-M. Fung, et al., Recent progress in two-dimensional nanomaterials for photocatalytic carbon dioxide transformation into solar fuels, *Mater. Today Sustain.* 9 (2020), 100037.
- [31] M. Zhao, et al., Recent advances in graphitic carbon nitride supported single-atom catalysts for oxygen conversion, *ChemCatChem* 13 (5) (2021) 1250–1270.
- [32] S. Büchele, et al., Tailoring nitrogen-doped carbons as hosts for single-atom catalysts, *ChemCatChem* 11 (12) (2019) 2812–2820.
- [33] Y. Xiong, et al., Single-atom Rh/N-doped carbon electrocatalyst for formic acid oxidation, *Nat. Nanotechnol.* 15 (5) (2020) 390–397.
- [34] Y. Zhu, et al., Unravelling the structure of electrocatalytically active Fe–N complexes in carbon for the oxygen reduction reaction, *Angew. Chem.* 126 (40) (2014) 10849–10853.

- [35] Y.J. Sa, et al., A general approach to preferential formation of active Fe–N x sites in Fe–N/C electrocatalysts for efficient oxygen reduction reaction, *J. Am. Chem. Soc.* 138 (45) (2016) 15046–15056.
- [36] J. Xie, et al., Highly selective oxidation of methane to methanol at ambient conditions by titanium dioxide-supported iron species, *Nat. Catal.* 1 (11) (2018) 889.
- [37] Z.Y. Wu, et al., Iron carbide nanoparticles encapsulated in mesoporous Fe–N-doped carbon nanofibers for efficient electrocatalysis, *Angew. Chem.* 127 (28) (2015) 8297–8301.
- [38] A. Savateev, et al., Discriminating catalytically active FeN x species of atomically dispersed Fe–N–C catalyst for selective oxidation of the C–H bond, *J. Am. Chem. Soc.* 139 (31) (2017) 10790–10798.
- [39] A. Savateev, et al., Potassium poly (heptazine imides) from aminotetrazoles: shifting band gaps of carbon nitride-like materials for more efficient solar hydrogen and oxygen evolution, *ChemCatChem* 9 (1) (2017) 167–174.
- [40] Z. Chen, et al., “The easier the better” preparation of efficient photocatalysts—metastable poly (heptazine imide) salts, *Adv. Mater.* 29 (32) (2017) 1700555.
- [41] A. Savateev, et al., Towards organic zeolites and inclusion catalysts: heptazine imide salts can exchange metal cations in the solid state, *Chemistry–Asian J.* 12 (13) (2017) 1517–1522.
- [42] F.M. Colombari, et al., Graphitic carbon nitrides as platforms for single-atom photocatalysis, *Faraday Discuss.* 227 (0) (2021) 306–320.
- [43] G. Song, F. Wang, X. Li, C–C, C–O and C–N bond formation via rhodium (iii)-catalyzed oxidative C–H activation, *Chem. Soc. Rev.* 41 (9) (2012) 3651–3678.
- [44] X. Wang, D. Leow, J.-Q. Yu, Pd (II)-catalyzed para-selective C–H arylation of monosubstituted arenes, *J. Am. Chem. Soc.* 133 (35) (2011) 13864–13867.
- [45] E. Lu, et al., Selective Hydroxylation of Benzene to Phenol over Fe nanoparticles encapsulated within N-doped carbon shells, *ACS Appl. Nano Mater.* 3 (9) (2020) 9192–9199.
- [46] X. Chen, et al., Fe–g-C₃N₄-catalyzed oxidation of benzene to phenol using hydrogen peroxide and visible light, *J. Am. Chem. Soc.* 131 (33) (2009) 11658–11659.
- [47] P. Xiao, et al., Consequences of Fe speciation in MFI zeolites for hydroxylation of benzene to phenol with H₂O₂, *Appl. Catal. A: Gen.* 579 (2019) 159–167.
- [48] M. Zhang, et al., Metal (hydr) oxides@ polymer core–shell strategy to metal single-atom materials, *J. Am. Chem. Soc.* 139 (32) (2017) 10976–10979.
- [49] D. Deng, et al., A single iron site confined in a graphene matrix for the catalytic oxidation of benzene at room temperature, *Sci. Adv.* 1 (11) (2015), e1500462.
- [50] Y. Pan, et al., Regulating the coordination structure of single-atom Fe–Nx/Cy catalytic sites for benzene oxidation, *Nat. Commun.* 10 (1) (2019) 4290.
- [51] Y.M. Alshammari, K. Hellgardt, Partial oxidation of n-hexadecane through decomposition of hydrogen peroxide in supercritical water, *Chem. Eng. Res. Des.* 93 (2015) 565–575.
- [52] P.E. Blöchl, O. Jepsen, O.K. Andersen, Improved tetrahedron method for Brillouin-zone integrations, *Phys. Rev. B* 49 (23) (1994) 16223.
- [53] G. Kresse, J. Furthmüller, Efficiency of ab-initio total energy calculations for metals and semiconductors using a plane-wave basis set, *Comput. Mater. Sci.* 6 (1996) 15f50.
- [54] G. Kresse, J. Furthmüller, Efficient iterative schemes for ab initio total-energy calculations using a plane-wave basis set, *Phys. Rev. B* 54 (16) (1996) 11169.
- [55] J.P. Perdew, K. Burke, M. Ernzerhof, Generalized gradient approximation made simple, *Phys. Rev. Lett.* 77 (18) (1996) 3865.
- [56] S. Grimme, et al., A consistent and accurate ab initio parametrization of density functional dispersion correction (DFT-D) for the 94 elements H–Pu, *J. Chem. Phys.* 132 (15) (2010), 154104.
- [57] H.J. Monkhorst, J.D. Pack, Special points for Brillouin-zone integrations, *Phys. Rev. B* 13 (12) (1976) 5188.
- [58] A. Savateev, et al., Potassium poly(heptazine imide): transition metal-free solid-state triplet sensitizer in cascade energy transfer and [3+2]-cycloadditions, *Angew. Chem. Int. Ed.* 59 (35) (2020) 15061–15068.
- [59] T.D. Kühne, E. Prodan, Disordered crystals from first principles I: Quantifying the configuration space, *Ann. Phys.* 391 (2018) 120–149.
- [60] H. Fei, et al., Atomic cobalt on nitrogen-doped graphene for hydrogen generation, *Nat. Commun.* 6 (1) (2015) 1–8.
- [61] L. Shi, et al., Photoassisted construction of holey defective g-C₃N₄ photocatalysts for efficient visible-light-driven H₂O₂ production, *Small* 14 (9) (2018) 1703142.
- [62] Y. Wang, et al., Synthesis of boron doped polymeric carbon nitride solids and their use as metal-free catalysts for aliphatic C–H bond oxidation, *Chem. Sci.* 2 (3) (2011) 446–450.
- [63] J. Li, et al., Atomically dispersed cobalt on graphitic carbon nitride as a robust catalyst for selective oxidation of ethylbenzene by peroxymonosulfate, *J. Mater. Chem. A* 9 (5) (2021) 3029–3035.
- [64] P. Zhang, et al., Selective oxidation of benzene to phenol by FeCl₃/mpg-C₃N₄ hybrids, *RSC Adv.* 3 (15) (2013) 5121–5126.
- [65] D. Wang, M. Wang, Z. Li, Fe-based metal–organic frameworks for highly selective photocatalytic benzene hydroxylation to phenol, *ACS Catal.* 5 (11) (2015) 6852–6857.
- [66] R.J. Schmidt, Industrial catalytic processes—phenol production, *Appl. Catal. A: Gen.* 280 (1) (2005) 89–103.
- [67] X. Ye, et al., Selective oxidation of benzene to phenol by Fe–CN/TS-1 catalysts under visible light irradiation, *Appl. Catal. B: Environ.* 152 (2014) 383–389.
- [68] S.M. Hosseini, et al., Au–Pd@ g-C₃N₄ as an efficient photocatalyst for visible-light oxidation of benzene to phenol: experimental and mechanistic study, *J. Phys. Chem. C* 122 (48) (2018) 27477–27485.
- [69] P. Devaraji, N.K. Sathu, C.S. Gopinath, Ambient oxidation of benzene to phenol by photocatalysis on Au/TiO₂. 98V0. 02O2: role of holes, *ACS Catalysis* 4 (9) (2014) 2844–2853.
- [70] O. Tomita, B. Ohtani, R. Abe, Highly selective phenol production from benzene on a platinum-loaded tungsten oxide photocatalyst with water and molecular oxygen: selective oxidation of water by holes for generating hydroxyl radical as the predominant source of the hydroxyl group, *Catal. Sci. Technol.* 4 (11) (2014) 3850–3860.
- [71] K.P. Bryliakov, E.P. Talsi, Active sites and mechanisms of bioinspired oxidation with H₂O₂, catalyzed by non-heme Fe and related Mn complexes, *Coord. Chem. Rev.* 276 (2014) 73–96.
- [72] K.M. Van Heuvelen, et al., One-electron oxidation of an oxoiron (IV) complex to form an [O=FeV=NR]⁺ center, *Proc. Natl. Acad. Sci. USA* 109 (30) (2012) 11933–11938.
- [73] A. Das, J.E. Nutting, S.S. Stahl, Electrochemical C–H oxygenation and alcohol dehydrogenation involving Fe-oxo species using water as the oxygen source, *Chem. Sci.* 10 (32) (2019) 7542–7548.
- [74] D.C. Lacy, et al., Formation, structure, and EPR detection of a high spin FeIV–Oxo species derived from either an FeIII–Oxo or FeIII–OH complex, *J. Am. Chem. Soc.* 132 (35) (2010) 12188–12190.
- [75] J. Cho, et al., Structure and reactivity of a mononuclear non-haem iron (III)–peroxo complex, *Nature* 478 (7370) (2011) 502–505.
- [76] T.H. Yosca, et al., Iron (IV) hydroxide pKa and the role of thiolate ligation in C–H bond activation by cytochrome P450, *Science* 342 (6160) (2013) 825–829.